




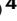





Dry hydroclimates in the late Palaeocene-early Eocene hothouse world

Received: 7 November 2023

Accepted: 6 August 2024

Published online: 15 August 2024



Victor A. Piedrahita ^{1,2,3,4}, Andrew P. Roberts ⁴, Eelco J. Rohling ^{5,6}, David Heslop ⁴, Xiang Zhao ⁴, Simone Galeotti ^{7,8}, Fabio Florindo ^{8,9}, Katharine M. Grant ⁴, Pengxiang Hu⁴ & Jinhua Li ^{1,2,3,10} ✉

Extreme global warming can produce hydroclimate changes that remain poorly understood for sub-tropical latitudes. Late Palaeocene-early Eocene (LPEE; ~58–52 Ma) proto-Mediterranean zones of the western Tethys offer opportunities to assess hydroclimate responses to massive carbon cycle perturbations. Here, we reconstruct LPEE hydroclimate conditions of these regions and find that carbon cycle perturbations exerted controls on orbitally forced hydroclimate variability. Long-term (~6 Myr) carbon cycle changes induced a gradual precipitation/moisture reduction, which was exacerbated by some short-lived (<200 kyr) carbon cycle perturbations that caused rapid warming and exceptionally dry conditions in western Tethyan continental areas. Hydroclimate recovery following the greatest short-lived global warming events took ~24–27 kyr. These observations support the notion that anthropogenically driven warming can cause widespread aridification with impacts that may last tens of thousands of years.

Human-driven greenhouse gas emissions induce detrimental environmental impacts that may last thousands of years if important climate change mitigation strategies are not adopted^{1,2}. Anthropogenic global warming is expected to cause substantial hydrological cycle variations that threaten water security in diverse regions^{3–5}. Model experiments have used historical data to suggest that continental Mediterranean zones—i.e., southern Europe and northern Africa—may experience intensified aridity in the next three decades^{3,6}. However, the severity and persistence of drought associated with different possible global warming scenarios may have been underestimated by model simulations^{4,5}. Geological hydroclimate reconstructions of sub-tropical Mediterranean regions indicate contrasting drier or wetter responses to diverse global warming events^{7–9}. Hence, the impacts of extreme climatic conditions on Mediterranean hydroclimates, and the

temporal extent of global warming influences on the hydrological cycle, remain poorly constrained.

The shared socio-economic pathway (SSP; see Tab. S1 for unabridged acronyms) 8.5 of the Intergovernmental Panel on Climate Change (IPCC) comprises massive carbon emissions and predicts a hothouse climate state (>5–10 °C temperature increase) over the next two centuries². This severe global warming scenario is predicted to cause major hydroclimate variations, ice melting, sea level rise, and triggering of negative carbon cycle feedbacks that can potentially extend the lifetime of human-induced global warming for more than 100 kyr^{2,10}. These projected conditions are roughly similar to those of the late Palaeocene-early Eocene (LPEE, ~58–52 Ma), which records multiple global warming events that produced SSP 8.5-like climatic scenarios^{2,11,12}. Although LPEE global warming events developed under

¹Key Laboratory of Deep Petroleum Intelligent Exploration and Development, Institute of Geology and Geophysics, Chinese Academy of Sciences, Beijing 100029, China. ²Laboratory for Marine Geology, Qingdao Marine Science and Technology Center, Qingdao 266237, China. ³Southern Marine Science and Engineering Guangdong Laboratory, Zhuhai 519082, China. ⁴Research School of Earth Sciences, Australian National University, ACT 2601 Canberra, Australia. ⁵Department of Earth Sciences, Utrecht University, Princetonlaan 8, 3584 CB Utrecht, The Netherlands. ⁶School of Ocean and Earth Science, University of Southampton, National Oceanography Centre, SO14 3ZH Southampton, UK. ⁷Dipartimento di Scienze Pure e Applicate, Università degli Studi di Urbino, 61029 Urbino, Italy. ⁸Institute for Climate Change Solutions, Via Sorchio, 61040 Frontone, Pesaro e Urbino, Italy. ⁹Istituto Nazionale di Geofisica e Vulcanologia, Via di Vigna Murata 605, 00143 Rome, Italy. ¹⁰College of Earth and Planetary Sciences, University of Chinese Academy Sciences, Beijing 100049, China.

✉ e-mail: lijinhua@mail.iggcas.ac.cn

contrasting continental configurations with respect to the current tectonic setting, and had slower carbon release rates compared to anthropogenic global warming^{11,13,14}, geological LPEE records have been interpreted to offer a suitable opportunity to assess potential global warming impacts of SSP 8.5-like climatic conditions on the hydrological cycle^{9,11,14–16}. Therefore, LPEE hydroclimate reconstructions of proto-Mediterranean areas can provide insights into hydrological cycle responses of sub-tropical regions to increased temperatures and can enable estimation of the typical duration of global warming controls on the hydrological cycle.

LPEE hothouse climates were characterised by orbitally forced carbon cycle/temperature variations on eccentricity and precession timescales^{17–19}. These orbitally paced patterns were superimposed upon a ~5-Myr-long temperature increase that correlates with decreasing stable oxygen ($\delta^{18}\text{O}$) and carbon ($\delta^{13}\text{C}$) isotope signals (Fig. 1a). This long-term carbon cycle perturbation resulted from a gradual organic carbon burial reduction and/or increased volcanic activity^{12,20}, and was punctuated by short-lived (<200 kyr) carbon cycle perturbations that systematically occurred under enhanced seasonal contrast conditions close to both long (~400 kyr) and short (~100 kyr) eccentricity maxima^{21–24}. Short-lived LPEE carbon cycle perturbations were associated with isotopically light carbon injections of different

magnitudes, which were triggered by orbitally forced and/or volcanism-related mechanisms^{24,25}. These events are recognised by negative carbon isotope excursions (CIEs) and include hyperthermals such as the Palaeocene-Eocene Thermal Maximum (PETM; ~56 Ma). This event was the largest hyperthermal and has been associated with a carbon release of 3000–10,000 Gt^{13,25}. Succeeding hyperthermals include the Eocene Thermal Maximum (ETM) 2 (~54 Ma) and ETM 3 (~53 Ma), which had considerably smaller environmental impacts and magnitudes than the PETM^{22,26}. For instance, carbon release estimates for the ETM 2 range only between ~2600 Gt and ~3800 Gt²⁶. Smaller LPEE carbon cycle perturbations also occurred between hyperthermals, and were called the F, H2, I1, I2, L1, and L2 events^{19,21,22} (Fig. 1a).

Short-lived LPEE carbon cycle perturbations have been divided into a peak phase, with temperature increases, ocean acidification, and major hydroclimate changes, and a succeeding recovery phase of accelerated carbon sequestration^{19,21–23} (Fig. S1). This period, which is marked by irreversible $\delta^{13}\text{C}$ transitions from more negative to more positive values, is assumed to have restored environmental changes induced by global warming to pre-event-like settings. Accelerated carbon removal occurred during the first ~6–26 kyr of the recovery phase due to optimisation of the oceanic biological pump^{19,27}. This

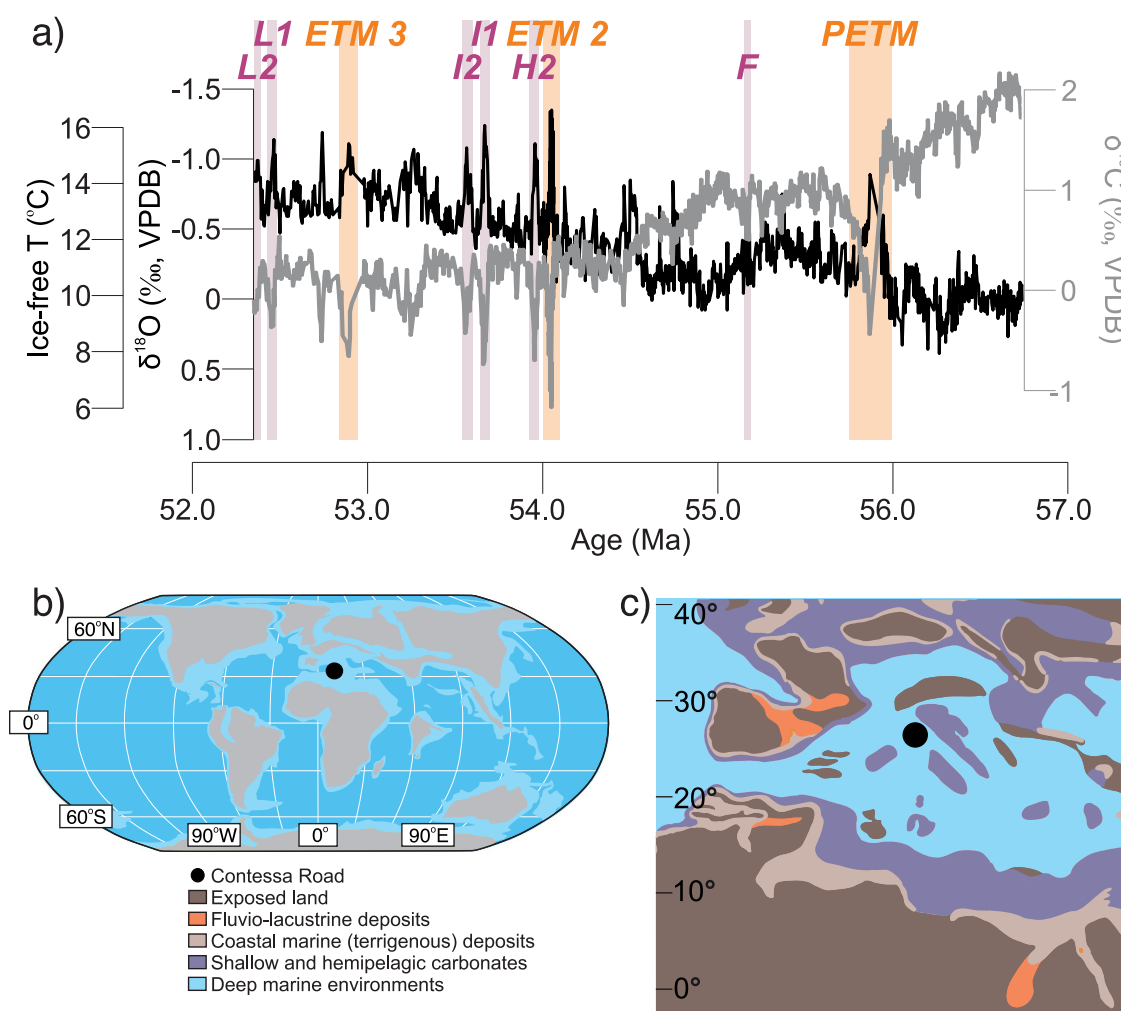


Fig. 1 | Late Palaeocene-early Eocene (LPEE) temperature reconstructions and Contessa Road location. **a** LPEE palaeotemperature, stable oxygen isotope ($\delta^{18}\text{O}$) and stable carbon isotope ($\delta^{13}\text{C}$) data from a global reference benthic foraminiferal record¹². Temperature estimates are relative to the 1961–1990 global mean. Hyperthermals (Palaeocene-Eocene Thermal Maximum (PETM), Eocene Thermal Maximum (ETM) 2 and ETM 3) and smaller carbon cycle perturbations are indicated

with orange and purple bands, respectively. **b** Global palaeogeographic reconstruction at ~56 Ma³⁹ with the Contessa Road location. **c** Palaeogeographic reconstruction of LPEE sedimentary environments across the western Tethys⁴². Exposed land (dark brown), fluvio-lacustrine deposits (orange), coastal marine (terrigenous) deposits (light brown), shallow and hemipelagic carbonates (purple), and deep marine environments (blue) are indicated.

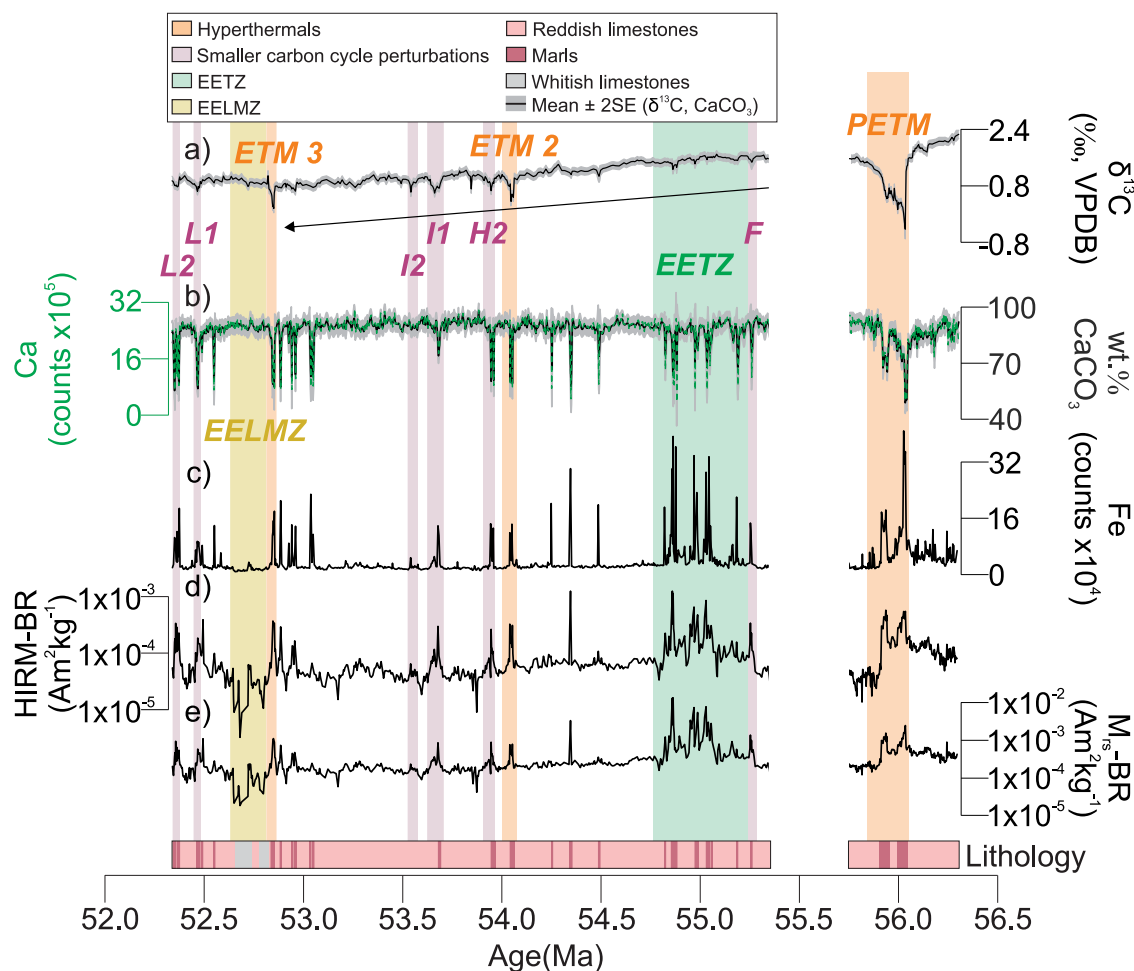


Fig. 2 | Contessa Road climate proxy and geochemical records. **a** Stable carbon isotope ($\delta^{13}\text{C}$)¹⁹, **b** Ca and CaCO_3 ¹⁹, **c** Fe, **d** bulk-rock hard isothermal remanent magnetisation (HIRM-BR), and **e** bulk-rock saturation remanent magnetisation ($M_{\text{S-BR}}$) records from Contessa Road (this study). $\delta^{13}\text{C}$ and CaCO_3 are presented in terms of mean (black) \pm 2 standard errors (2SE) (shaded grey bands). Hyperthermals (Palaeocene-Eocene Thermal Maximum (PETM), Eocene Thermal Maximum

(ETM) 2 and ETM 3), smaller carbon cycle perturbations, the early Eocene terrigenous zone (EETZ), and the early Eocene low magnetisation zone (EELMZ) are indicated with orange, purple, green and yellow bands, respectively. The arrow in (a) indicates the long-term $\delta^{13}\text{C}$ decrease. Lithology is indicated at the bottom of the figure with reddish (pink) and whitish limestones (grey) and marls (red). Source data are provided as a Source Data file.

process was enhanced in proportion to the initial magnitude of the light carbon injection that triggered each short-lived LPEE global warming event, and its duration (~6–26 kyr) coincided with that of the ocean acidification recovery¹⁹. However, the incidence of carbon sequestration on other processes, such as LPEE hydroclimate variability, is still poorly understood, partially because hydroclimate recovery timescales are yet to be constrained.

Continental hydroclimate reconstructions indicate global wet-becomes-wetter and dry-becomes-drier hydroclimate responses (hereafter called wet-wetter and dry-drier) during peak PETM and ETM 2 conditions^{9,11,14,28}. This pattern, which would be expected to be especially intensified over the ocean by increased lower-tropospheric water vapour transport²⁹, has been associated with polar amplification, atmospheric circulation and temperature gradient changes induced by LPEE global warming⁹. PETM and ETM 2 dry-drier hydroclimate responses have been found over some sub-tropical continental interiors as a result of reduced moisture divergence and weak meridional temperature gradients^{9,28,30–35}. These regions have been considerably less studied than high and tropical latitudes, where wet-wetter hydroclimate responses have been identified^{28,36–39}; however, some sedimentary records also provide evidence of contrasting hydrological responses between the PETM and succeeding short-lived carbon cycle perturbations (i.e., dry-becomes-wetter⁴⁰).

LPEE sub-tropical regions include proto-Mediterranean zones of western Tethyan continental areas, where dry hydroclimates with intermittent extreme precipitation events are recorded in the PETM^{28,30–32,34}. These areas were located at roughly similar latitudes as modern Mediterranean zones^{41–44}, which are influenced by seasonal precipitation systems (e.g., monsoons and winter storm tracks) that are sensitive to pressure and moisture divergence changes^{45,46}. Spatial contrasts in the responses of those seasonal precipitation systems to increased temperatures can generate wetter or drier conditions across different modern southern Europe and northern Africa^{3,45,46}. During the Neogene-Quaternary, orbitally forced precipitation patterns caused important Mediterranean hydroclimate fluctuations⁴⁷. However, the possibility of underlying control by orbital forcing and global warming on LPEE proto-Mediterranean hydroclimates remains elusive.

LPEE proto-Mediterranean hydroclimate variability can be recorded by detrital minerals contained within western Tethyan marine sedimentary sections, such as the sub-tropical Contessa Road section (Fig. 1b; see Methods). This section has records of LPEE carbon cycle perturbations in marine pelagic carbonates of the Scaglia Rossa Formation¹⁹ (Fig. 2a, S1). This unit contains limestones that alternate with marls, which usually coincide with short-lived LPEE carbon cycle perturbations¹⁹. These marly layers contain low planktonic and high agglutinated foraminifera contents and had either reduced or similar

sedimentation rates compared to limestones^{19,21}. These features indicate that Contessa Road sedimentation depended mainly on biogenic CaCO_3 deposition/dissolution patterns, which is corroborated by orbitally driven CaCO_3 dissolution cycles that have been associated with ocean/atmosphere light carbon concentration shifts^{21,22,24} (Fig. S2). Despite the minor terrigenous component of Contessa Road sediments^{21,41}, this section also contains detrital minerals within aeolian dust fractions, which are interpreted as erosion products from western Tethyan continental rock massifs in northern Africa and southern Europe^{21,42–44}. The terrigenous fraction of Scaglia Rossa carbonates includes haematite, maghemite, and magnetite^{44,48,49}, which serve as proxies for continental hydroclimate variability^{32,50,51}. Nevertheless, the relationship between hydrological cycle variations recorded by these minerals and LPEE global warming events has yet to be investigated. Here, we characterise Contessa Road sedimentation patterns, with a focus on magnetic minerals, to reconstruct western Tethyan continental hydroclimates. We present ~4 Myr-long high-resolution X-ray fluorescence (XRF) and rock magnetic records (see Methods) to assess the influence of orbital controls on the LPEE hydrological cycle, and to explore the impacts of both long-term climatic trends and short-lived carbon cycle perturbations on proto-Mediterranean hydroclimates. Our observations offer opportunities to gauge pre-anthropogenic hydroclimate recovery timescales, which provides insights into potential hydroclimate responses of Mediterranean regions to a hot-house SSP 8.5 global warming scenario.

Results

Contessa road CaCO_3 sedimentation

The Contessa Road section mainly consists of reddish limestones with high biogenic contents (Ca and CaCO_3), and low detrital element (e.g., Fe, Ti, Si, Al, Zr and Rb) and bulk-rock (BR) magnetic mineral concentration parameter values (e.g., BR saturation remanent magnetisation (M_{rs}), and BR hard isothermal remanent magnetisation (HIRM)). These rocks alternate with reddish marls with low Ca and CaCO_3 contents, and high detrital element and BR magnetic mineral concentration parameter values (Fig. 2b–e, S3, S4).

Contessa Road contains two intervals that differ from the typical alternating reddish limestone/ marl sedimentation pattern. The first is a ~600 kyr-long interval after the F event, which is referred to here as the early Eocene terrigenous zone (EETZ). This interval has the highest detrital element and BR magnetic mineral concentrations and contains several consecutive marls that do not coincide with major CIE events (Fig. 2). The second anomalous interval spans ~200 kyr following the ETM 3. We refer to this period as the early Eocene low magnetisation zone (EELMZ; Supplementary information), which contains whitish limestones that record the lowest BR magnetic mineral concentration values at Contessa Road (Fig. 2d, e, S4).

Contessa road magnetic minerals

Magnetic mineral assemblages of Scaglia Rossa carbonates consist of a mixture of high and low coercivity phases^{43,44,48}. Temperature-dependent magnetic susceptibility (χ -T) curves for 7 of 10 representative Contessa Road samples (see Methods) contain a gradual χ drop during heating from ~300 °C, and a single cooling peak at ~450–500 °C (Fig. 3, S5, S6). These features are compatible with transformation of pedogenic fine-grained maghemite into haematite⁵². An ETM 2 sample has no indication of a χ drop at ~300 °C; nevertheless, that χ -T curve has a ~615–630 °C heating drop that is indicative of maghemite⁵³, which is present in almost all Contessa Road samples (Fig. 3, S5, S6). χ -T curves also contain drops at ~580 °C for three samples, which indicate that magnetite is present in reduced proportions compared to maghemite (Fig. 3b, d). Three-axis thermal demagnetisation results⁵⁴ for representative Contessa Road samples (see Methods) typically reveal gradual magnetisation drops to 675 °C for all axes (Fig. 3a–e), which is diagnostic of pedogenic red pigmentary haematite⁵⁵. This

mineral gives reddish hues to the Scaglia Rossa carbonates^{44,48}, which persists across most Contessa Road limestones and marls (Fig. 4a). Scanning electron microscope (SEM) imaging and SEM-based energy dispersive X-ray spectroscopy (EDXS) analyses indicate that Fe-Al-rich minerals (e.g., maghemite, magnetite and red pigmentary haematite) appear in the clay fraction surrounding Ca-rich bioclasts (Fig. 4b–f, S7). Visual observations (Fig. 4a) and high-temperature rock magnetic experiments suggest that red pigmentary haematite is not present in the whitish carbonates of the EELMZ. Three-axis thermal demagnetisation results for this interval reveal a magnetisation drop at ~675 °C for the hard axis, which is interpreted to reflect the presence of specular haematite⁵⁵ (Fig. 3). This behaviour is not identified in other samples. In the EELMZ, a magnetisation drop also occurs for all axes at ~80 °C, which indicates the presence of goethite exclusively in this Contessa Road interval⁵⁴ (Fig. 3f).

The above rock magnetic experiments reveal that high coercivity magnetic mineral assemblages at Contessa Road mainly contain pigmentary haematite, while low coercivity magnetic mineral assemblages predominantly consist of maghemite although some magnetite is also present. Variability in the concentration of these minerals is estimated here on a carbonate free basis (CFB) (see Methods). CFB calculations remove CaCO_3 sedimentation controls on magnetic mineral concentration parameters⁵⁰, which allows clear identification of magnetic mineral content changes at Contessa Road (Fig. 5, S8). M_{rs} -CFB reflects concentration variations of all magnetic minerals, which indicates a long-term LPEE magnetic mineral concentration decrease (transition from red to pink dots in Fig. 5a) punctuated by the highest and lowest M_{rs} -CFB values during the EETZ and EELMZ, respectively (Fig. 5a). Haematite content variations are identified using HIRM-CFB. In contrast to M_{rs} -CFB, HIRM-CFB initially has a gradually increasing trend before the PETM that reaches maximum values across PETM marls (Fig. 5b). High HIRM-CFB values at the PETM peak are followed by an abrupt drop that coincides with limestones that mark the PETM recovery (change from red to pink dots in Fig. 5b). The PETM interval is then followed by an early Eocene haematite content decrease with the lowest values across the EELMZ and slight increases during some short-lived carbon cycle perturbations (Fig. 5b). Maghemite and magnetite content variations are recognised using anhysteretic remanent magnetisation (ARM). ARM-CFB decreases gradually from before the PETM, with lowest values across PETM marly layers. This gradual decrease is punctuated by limestones with pre-PETM ARM-CFB values (Fig. 5c). The PETM interval is then followed by a long-term early Eocene trend toward more negative ARM-CFB values (transition from red to pink dots in Fig. 5c). ARM-CFB decreases are also identified during some short-lived carbon cycle perturbations.

Magnetic mineral compositional variations at Contessa Road are estimated using coercivity of remanence (B_{cr}) and S-ratio (Fig. 5d, e, S9). High B_{cr} and low S-ratio values are interpreted to reflect the compositional dominance of haematite, while low B_{cr} and high S-ratio values indicate the compositional predominance of maghemite and magnetite^{50,51}. B_{cr} and S-ratio reveal a gradual transition from predominantly low pre-PETM coercivities to higher coercivities in PETM marls (Fig. 5d, e). These trends culminate in an abrupt change to low B_{cr} and high S-ratios in limestones that mark the PETM recovery (Fig. 5d, e). The PETM interval is then followed by a long-term compositional transition from low to high coercivities in the early Eocene. However, high B_{cr} and low S-ratio values across most short-lived carbon cycle perturbations and during the EELMZ interrupt this pattern (Fig. 5d, e).

Discussion

Origin of Contessa Road magnetic minerals

The Contessa Road section contains magnetic minerals that have been interpreted to be mainly produced in terrestrial environments^{32,50,51,56}. However, diverse authigenic processes have also been suggested as

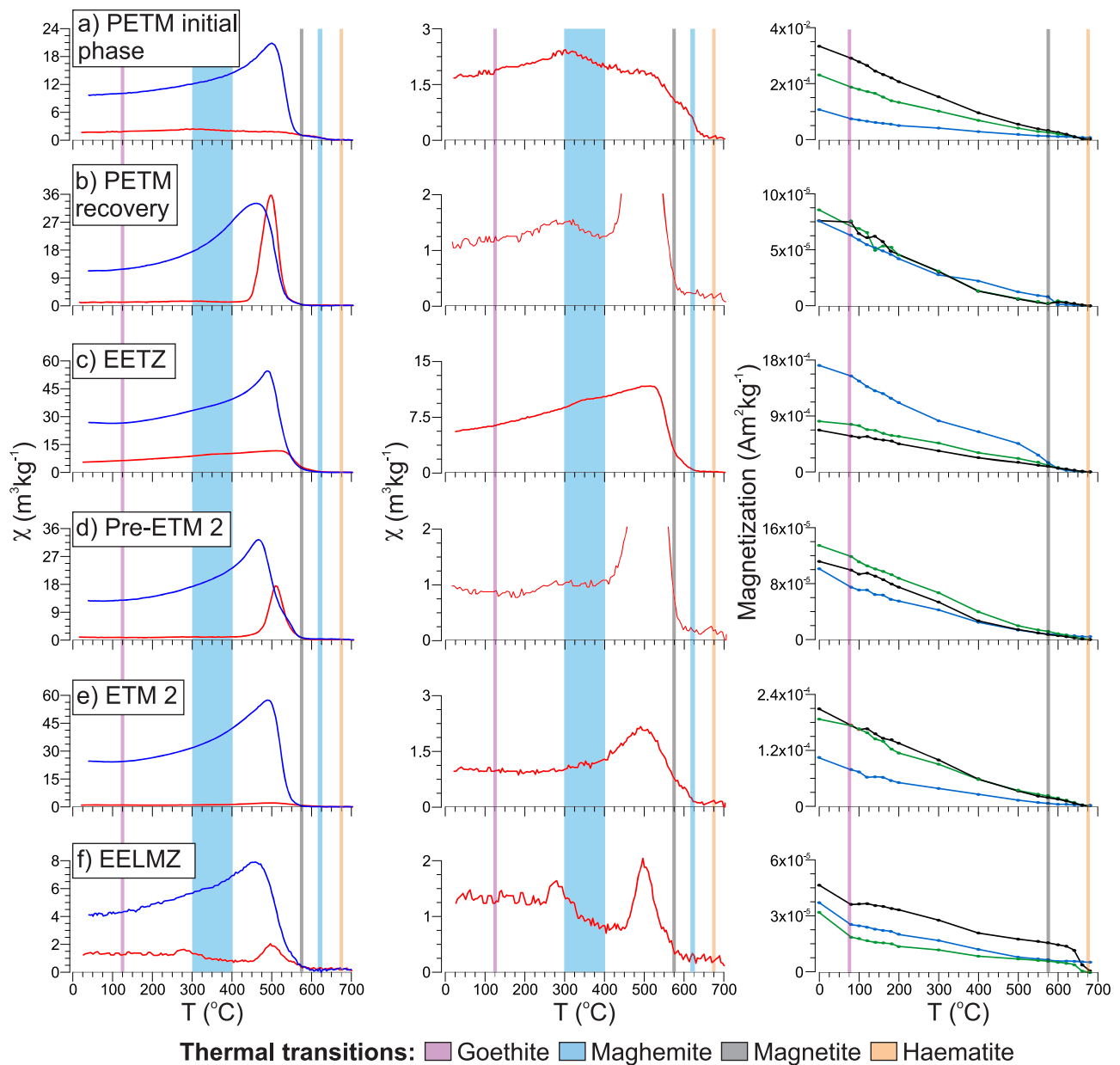


Fig. 3 | High-temperature magnetic results. Magnetic susceptibility-temperature (χ -T) curves with heating and cooling (left), heating-only curves (centre) and three-axis thermal demagnetisation results of an isothermal remanent magnetisation (right) for representative Contessa Road samples of **a** the Palaeocene-Eocene Thermal Maximum (PETM) initial phase, **b** PETM recovery, **c** early Eocene terrigenous zone (EETZ), **d** Pre-Eocene Thermal Maximum 2 (ETM 2), **e** ETM 2, and **f** early

Eocene low magnetisation zone (EELMZ). The cooling (blue) and heating (red) curves in χ -T experiments (left) are indicated. The hard-, medium- and soft-axis in three-axis demagnetisation results (right) are indicated by black, green, and blue lines, respectively. Circles represent thermal demagnetisation steps. Thermal transitions for magnetic minerals are indicated by purple (goethite), blue (maghemite), grey (magnetite) and orange (haematite) bars that cross all plots.

possible magnetic mineral formation mechanisms within the Scaglia Rossa Formation^{44,48,57}. The Cretaceous sequence of these carbonates has alternating reddish and whitish colours that indicate haematite presence or absence, respectively⁵⁷. This pattern was used to propose that Scaglia Rossa haematite was a diagenetic product of a goethite precursor⁵⁷. Haematite and maghemite were interpreted to form during oxic periods, while time intervals with reducing conditions inhibited formation of these minerals⁵⁷. Abrajevitch et al.⁴⁸ suggested a similar haematite formation mechanism but at the expense of Fe-rich oxyhydroxides within Scaglia Rossa aeolian dust fractions. A reducing environment implies preferential magnetite and maghemite dissolution over haematite^{48,57,58}, as identified at the Cretaceous/Palaeogene (K/Pg) boundary in whitish Scaglia carbonates⁴⁸. Our whitish EELMZ carbonates contain goethite and maghemite and lack pigmentary

haematite (Figs. 3f, 5c), which is incompatible with oxic and reducing condition alternations as maghemite/haematite formation mechanisms⁵⁷. Preferential dissolution of low coercivity minerals is also possible due to organic matter degradation and microbial oxidant consumption in organic-rich sediments⁵⁸. Contessa Road fossil and sedimentary assemblages do not provide evidence of significant organic-rich sediments inputs following the K/Pg boundary⁴⁴. Furthermore, detailed rock magnetic measurements (e.g., first-order reversal curves) from Palaeogene Contessa Road reddish carbonates do not contain reductive diagenesis signatures (e.g., magnetic Fe sulphide occurrences^{44,58}). Therefore, we interpret LPEE Contessa Road haematite and maghemite to be mainly of detrital origin.

Given the present-day Contessa Road location, post-depositional alteration of Fe-rich minerals could also be a potential

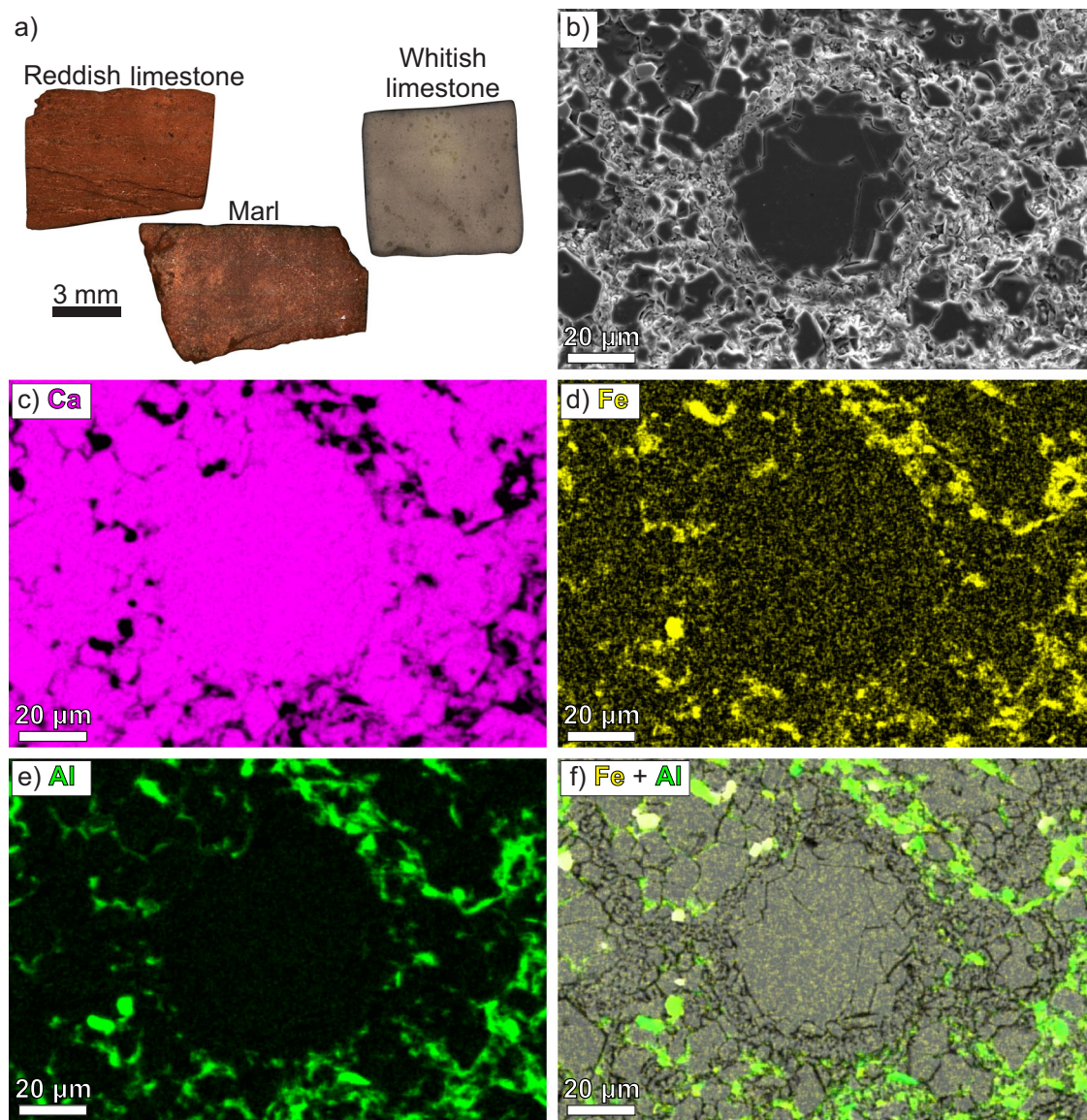


Fig. 4 | Scanning electron microscope (SEM) analyses. **a** Photographs of representative Contessa Road samples. **b** Backscattered electron image of a reddish limestone obtained with an in-lens T1 detector. False colour elemental maps of **c** Ca,

d Fe and **e** Al of a reddish limestone. **f** Backscattered electron image from **(b)**, with superimposed Fe (yellow) and Al (green) false colour maps.

maghemite and haematite formation mechanism⁵⁹. If this were the case, then increased magnetic mineral contents would have resulted in haematite-rich magnetic mineral fractions due to the greater availability of material for oxidation⁵⁵. Such a pattern contrasts with the long-term compositional change and magnetic mineral content reduction at Contessa Road (Fig. 5), which implies that mineral alteration is not a significant magnetic mineral formation process there and supports our argument for a detrital origin of Contessa Road magnetic minerals.

A detrital origin of Contessa Road haematite and maghemite suggests the occurrence of a widely recognised ferrihydrite→maghemite→haematite transformation in western Tethyan continental areas^{55,56}. Ferrihydrite ($\text{Fe}_5\text{HO}_8 \cdot 4\text{H}_2\text{O}$) is a common iron-oxide precursor, and its occurrence implies that wet periods with increased physical/chemical weathering generated erodible material⁵⁶. Gradual ferrihydrite dehydration produces maghemite and ultimately haematite in dry settings³⁵. Thus, magnetic minerals at Contessa Road reveal a dynamic LPEE proto-Mediterranean hydroclimate that consists of a dry setting with intermittent wetter conditions^{9,28,30–35}.

A few LPEE Contessa Road samples also contain magnetite. This mineral may have biological and detrital origins in the Scaglia Rossa Formation^{44,48}. Early Palaeogene Contessa Road carbonates have been interpreted to contain mainly biogenic magnetite, while the upper Cretaceous Scaglia Rossa record contains biogenic and detrital magnetite in similar proportions^{44,48}. Contessa Road biogenic magnetite occurrences have been inferred only from low coercivity central ridges in first-order reversal curve diagrams and from isothermal remanent magnetisation acquisition curves with ~20–50 mT coercivity components^{44,48}. However, these features are also compatible with the presence of detrital magnetite and maghemite⁶⁰. Early Palaeogene isothermal remanent magnetisation acquisition curves differ from those of the LPEE interval, and even if biogenic magnetite is present in the LPEE Contessa Road record, its contribution would be reduced compared to detrital magnetite (Figs. S10–S12; see Supplementary information). Furthermore, strong evidence for biogenic magnetite with chain or partially collapsed chain arrangement (i.e., from transmission electron microscope imaging^{60,61}) is lacking for the Contessa Road section. Therefore, we interpret magnetite within the LPEE

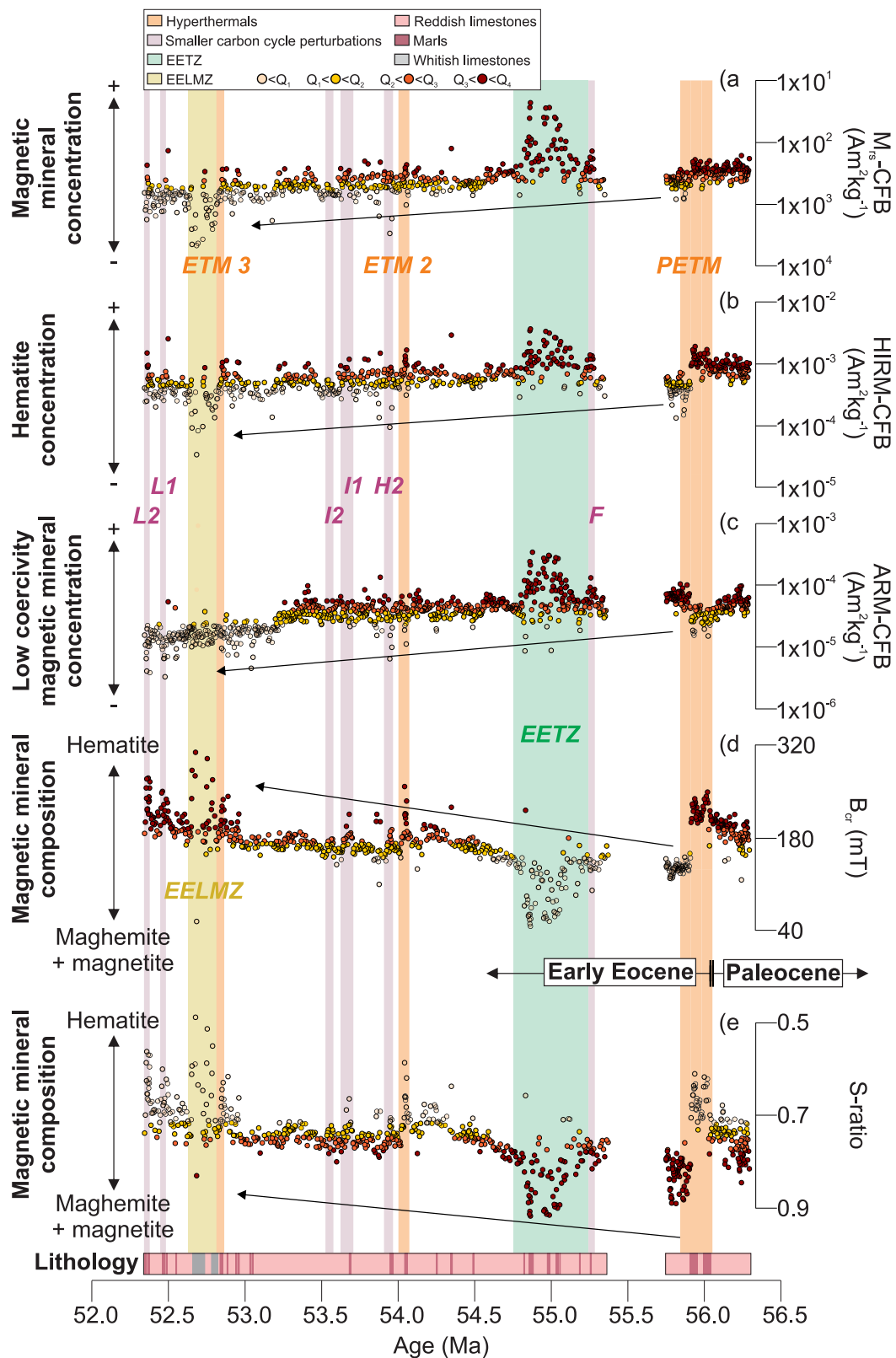


Fig. 5 | Magnetic mineral composition and concentration variations in a carbonate free basis (CFB) at Contessa Road. a Saturation remanent magnetisation (M_{rs})-CFB, **b** hard isothermal remanent magnetisation (HIRM)-CFB, **c** anhysteretic remanent magnetisation (ARM)-CFB, **d** coercivity of remanence (B_{cr}) and **e** S-ratio. Data were divided into quartiles (Q_1 , Q_2 , Q_3 and Q_4) to indicate variability. Long-term trends are indicated with arrows. Hyperthermals (Palaeocene-Eocene Thermal

Maximum (PETM), Eocene Thermal Maximum (ETM) 2 and ETM 3), smaller carbon cycle perturbations, the early Eocene terrigenous zone (EETZ), and the early Eocene low magnetisation zone (EELMZ) are indicated with orange, purple, green and yellow bands, respectively. Lithology is presented at the bottom of the figure with reddish (pink) and whitish (grey) and marls (red). Source data are provided as a Source Data file.

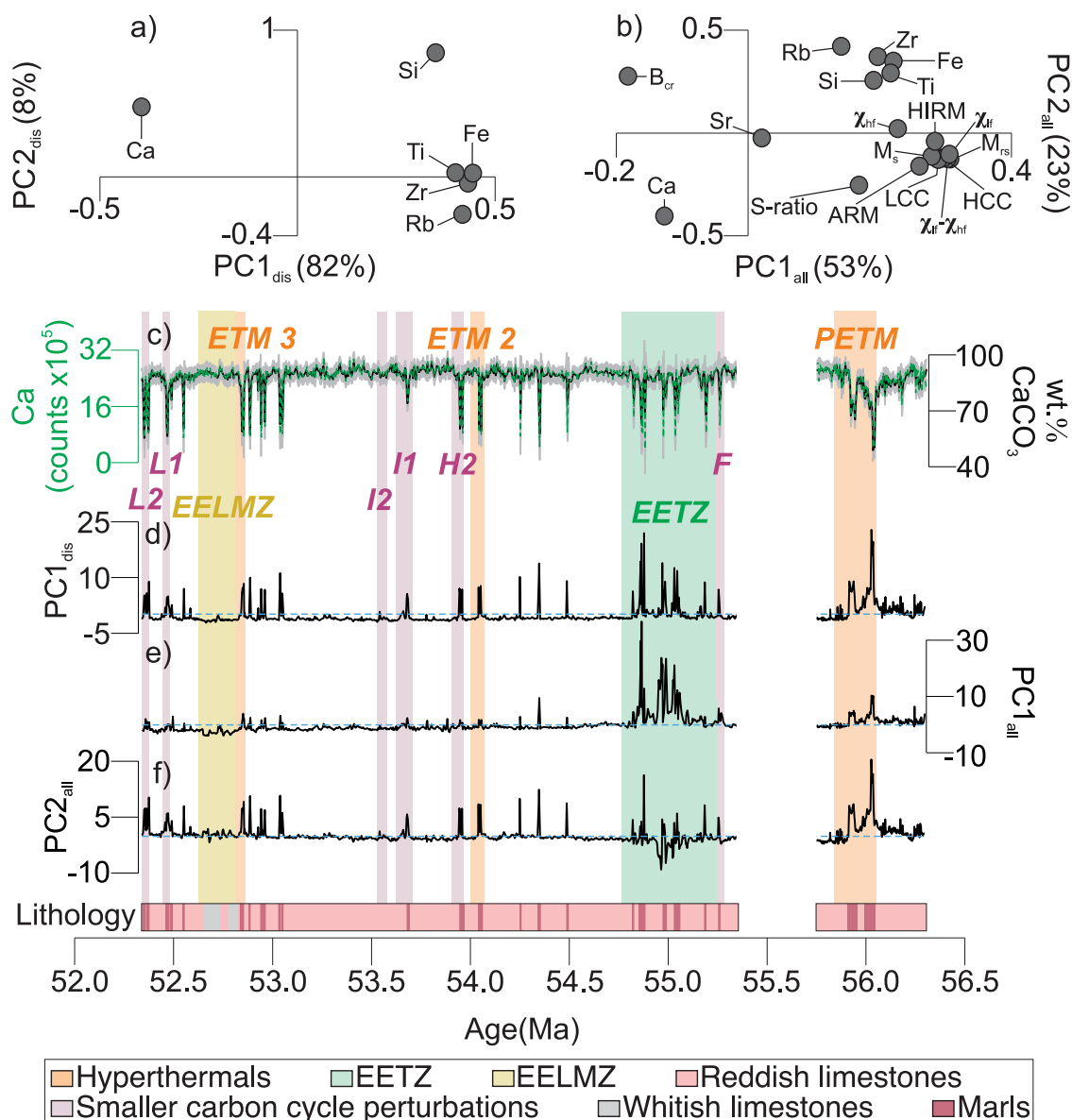


Fig. 6 | Principal component analysis (PCA). **a** $PC1_{dis}$ - $PC2_{dis}$ plot. **b** $PC1_{all}$ - $PC2_{all}$ plot. PCA_{all} includes all carbonate free basis (CFB) magnetic mineral concentration parameters (see Supplementary information). Bulk-rock (BR) magnetic mineral concentration parameters were not used. In **b**, CFB labels were removed for clarity. HCC and LCC correspond to the unmixed high coercivity component and the most significant low coercivity component 1, respectively (see Fig. S10; Supplementary information). **c** Ca and $CaCO_3$ records. $CaCO_3$ is presented in terms of mean (black) ± 2 standard errors (2SE; grey shaded bands)¹⁹. **d** $PC1_{dis}$, **e** $PC1_{all}$, **f** $PC2_{all}$ scores.

Hyperthermals (Palaeocene-Eocene Thermal Maximum (PETM), Eocene Thermal Maximum (ETM) 2 and ETM 3), smaller carbon cycle perturbations, the early Eocene terrigenous zone (EETZ), and the early Eocene low magnetisation zone (EELMZ) are indicated with orange, purple, green and yellow bands, respectively. The dashed blue line in **(d)**, **(e)**, and **(f)** indicates 0 in the y-axis. Lithology is presented at the bottom of the figure with reddish (pink) and whitish limestones (grey) and marls (red).

Contessa Road record to mainly have a terrigenous origin. This suggests that the Contessa Road rock magnetic record reflects primarily detrital magnetic mineral contents and compositional variations^{43,44,48,49}.

Biogenic versus detrital controls on Contessa Road sediment accumulation

Despite the terrigenous origin of magnetic minerals, biogenic $CaCO_3$ deposition/dissolution have been suggested as the main controlling mechanisms of Contessa Road sediment accumulation^{21,24,43,44,49,62}. Here, we assess $CaCO_3$ dissolution changes at Contessa Road with principal component analysis (PCA; see Methods) of Ca and detrital elements (referred to here as PCA_{dis}). PCA_{dis} reveals a major component that accounts for 82% of data variance ($PC1_{dis}$) and a second

component that only accounts for 8% of data variance ($PC2_{dis}$). $PC1_{dis}$ - $PC2_{dis}$ relationships confirm major $CaCO_3$ dissolution controls on Contessa Road sediment accumulation with negative correlations between Ca and detrital element loadings (Fig. 6a, S13a, Tab. S2), and with coincidence between $PC1_{dis}$ score increases and $CaCO_3$ decreases^{21,24,43,44,49,62} (Fig. 6c, d, S13a, Tab. S2). PCA of XRF elements, CFB magnetic concentration parameters, B_{cr} , and S-ratio (referred to here as PCA_{all}) yields a $PC1_{all}$ (53% of data variance; Fig. 6b). $PC1_{all}$ includes positive detrital element loadings that anti-correlate with Ca and correlate poorly with the negative B_{cr} loading, and with positive S-ratio and CFB magnetic mineral concentration parameter loadings. S-ratio and CFB magnetic mineral concentration parameter loadings anti-correlate with B_{cr} and have weak correlations with Ca (Fig. 6b, S13b, Tab. S2). These patterns suggest that positive $PC1_{all}$ scores reveal

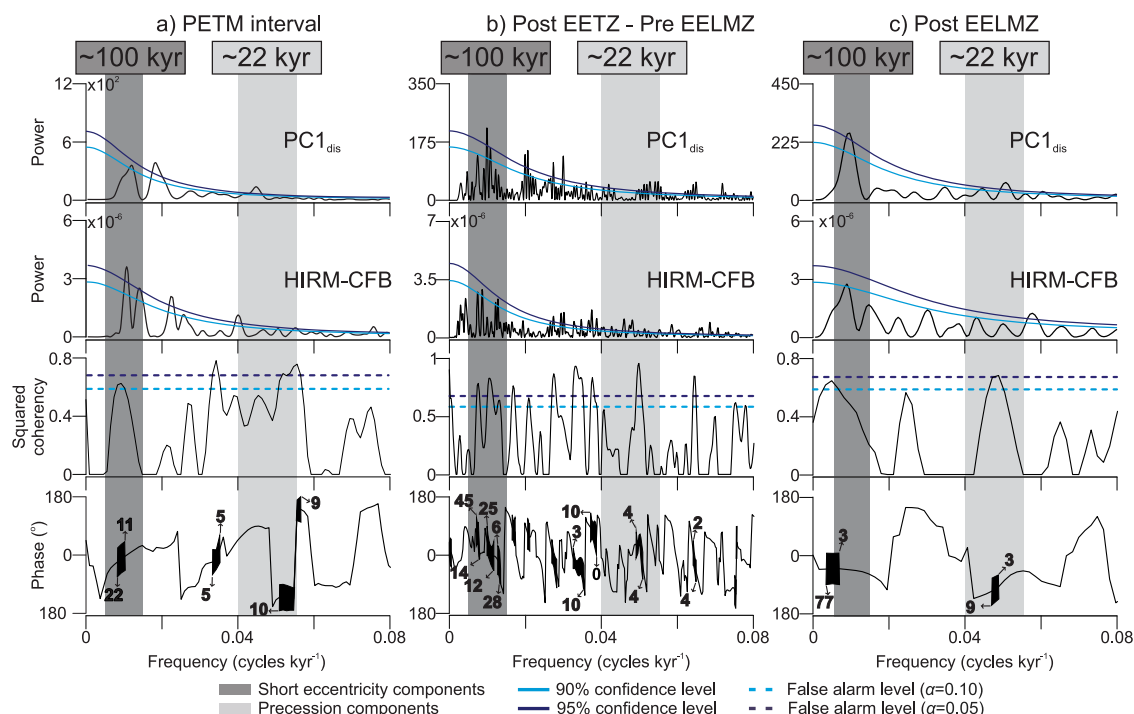


Fig. 7 | Spectral analysis. Power spectra (periodograms in the 1st and 2nd rows), squared coherency spectra (3rd row) and phase spectra (4th row) for PC1_{dis} and hard isothermal remanent magnetisation in a carbonate free basis (HIRM-CFB) for different Contessa Road intervals. **a** The Palaeocene-Eocene Thermal Maximum (PETM), **b** the post early Eocene terrigenous zone-pre early Eocene low magnetisation zone (post EETZ-Pre EELMZ) and **c** the post early Eocene low magnetisation zone (EELMZ) define the intervals in which spectral analyses were carried out. 90% and 95% confidence levels in periodograms are indicated by sky blue and dark blue

lines, respectively. False alarm levels $\alpha = 0.10$ and 0.05 in squared coherency spectra are indicated by sky blue and dark blue dashed lines, respectively. Black shapes in phase spectra represent lag/lead relationships of PC1_{dis} with respect to HIRM-CFB. Maximum and minimum lag/lead relationships are indicated in kyr by numbers next to black shapes in phase spectra. Associated frequencies of short eccentricity and precession are indicated by dark grey and light grey bands, respectively. Short eccentricity (~100 kyr) and precession (~22 kyr) periods are related to spectral peaks over the 90%-95% confidence levels.

enhanced CaCO₃ dissolution accompanied by high magnetic mineral inputs with increased low coercivity mineral contents (i.e., magnetite, maghemite) but reduced high coercivity fractions (Fig. 6e).

In contrast to PCA_{dis}, PCA_{all} reveals a significant second PCA component (PC2_{all}) that accounts for 23% of data variance (Fig. 6b). PC2_{all} has positive loadings for B_{cr} and detrital elements, and negative loadings for S-ratio, CFB magnetic mineral concentration parameter, and Ca (Fig. 6b, S13b, Tab. S2). These correlations suggest that PC2_{all} positive scores indicate enhanced CaCO₃ dissolution accompanied by reduced magnetic mineral inputs; however, magnetic mineral fractions isolated in PC2_{all} are compositionally dominated by high coercivity minerals (Fig. 6f). More pronounced PC2_{all} peaks with respect to PC1_{all} across short-lived carbon cycle perturbations suggest that CaCO₃ dissolution was preferentially coincident with haematite enrichments (Fig. 6e, f), which is confirmed by S-ratio and B_{cr} values (Fig. 5d, e). In contrast to positive values, PC2_{all} negative scores can be associated with enhanced CaCO₃ preservation and high terrigenous material inputs enriched in low coercivity minerals. Pronounced negative PC2_{all} peaks are identified exclusively in intervals of good CaCO₃ preservation during the EETZ (Fig. 6e, S14), which contains the highest detrital inputs across the LPEE Contessa Road record according to the CFB magnetic mineral concentration parameters (Fig. 5a–c). This pattern reveals that CaCO₃ deposition was not disturbed even when detrital inputs increased substantially (Figs. 5a–c, 6e, S14); therefore, we infer that terrigenous dilution was insignificant and did not play an important role in Contessa Road sediment accumulation^{19,21}. This is consistent with calcareous nanofossil assemblages and sedimentation rate variations, which indicate that, although Contessa Road had terrigenous inputs from western Tethyan continental regions^{42,49}, CaCO₃ deposition and

dissolution were prevailing drivers of sediment accumulation there^{21,24,43,44,62}.

Orbitally forced LPEE hydroclimate variability in the western Tethys

Orbitally forced LPEE carbon cycle and temperature changes have been suggested as drivers of CaCO₃ sedimentation and hydroclimate variability at diverse locations^{15,16,22}. Drier/wetter variations in LPEE western Tethyan continental areas, as inferred from the Contessa Road magnetic mineral assemblage, may be similar to those of well-documented Neogene-Quaternary Mediterranean regions, where orbitally driven mechanisms controlled dry/wet variability^{47,63,64}. Specifically, orbital controls on Contessa Road sedimentation are indicated by enhanced CaCO₃ dissolution during long eccentricity, short eccentricity, and precession maxima^{21,24}. We confirm the presence of those orbitally controlled CaCO₃ dissolution cycles with statistically significant spectral peaks (>90–95% confidence levels) at short eccentricity and precession periods in PC1_{dis} (Fig. 7, S15; see Methods). Similar spectral peaks in HIRM-CFB also reveal orbital controls on haematite deposition (Figs. 7, 8, S15). Squared coherency spectra of PC1_{dis} and HIRM-CFB, with significant peaks above false-alarm levels ($\alpha = 0.05$ and 0.10 ; Fig. 7) at short eccentricity and precession periods, corroborate the presence of these orbital signatures. Some peaks in the PC1_{dis} and HIRM-CFB power spectra may be related to obliquity; however, those peaks do not appear consistently across Contessa Road, which is confirmed by squared coherency analyses (Fig. 7). Hence, obliquity is not further assessed in detail here.

Orbital signals in PC1_{dis} represent coupled CaCO₃/δ¹³C variations that were also used for Contessa Road age model development¹⁹ (see Methods). Thus, peaks and troughs of the filtered PC1_{dis} short

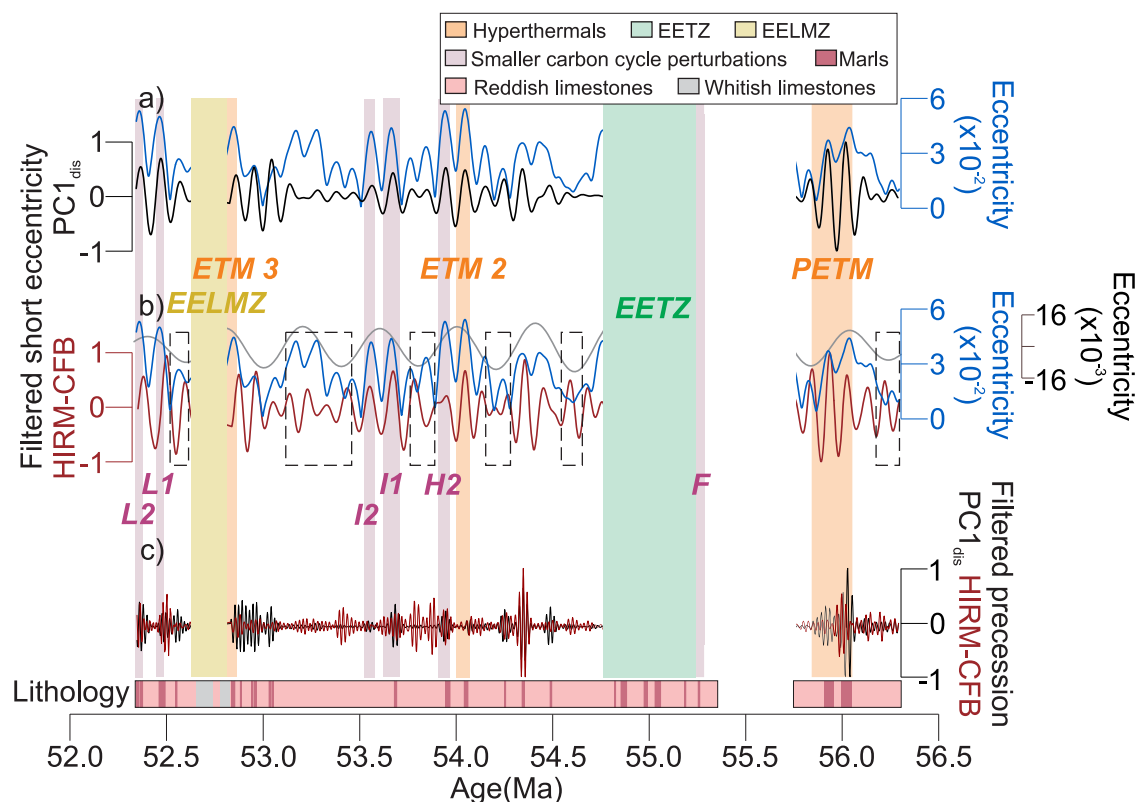


Fig. 8 | Orbital signals. Short (blue) and long (grey) eccentricity signals of the ZB18a astronomical solution²³, and filtered short eccentricity signals of (a) $PC1_{dis}$ and (b) hard isothermal remanent magnetisation in a carbonate free basis (HIRM-CFB). Intervals in which the filtered HIRM-CFB short eccentricity signal does not coincide well with the ZB18a astronomical solution²³ are indicated by rectangles with dashed black lines. c Filtered precession signals of $PC1_{dis}$ (black) and HIRM-

CFB (brown). Hyperthermals (Palaeocene-Eocene Thermal Maximum (PETM), Eocene Thermal Maximum (ETM) 2 and ETM 3), smaller carbon cycle perturbations, the early Eocene terrigenous zone (EETZ), and the early Eocene low magnetisation zone (EELMZ) are indicated with orange, purple, green and yellow bands, respectively. Lithology is presented at the bottom of the figure with reddish (pink) and whitish limestones (grey) and marls (red).

eccentricity signal coincide with those of the ZB18a astronomical solution²³ (Fig. 8a; see Methods). There are no available LPEE astronomical solutions against which we can compare the filtered $PC1_{dis}$ precession signal. However, multiple studies have identified precession in $CaCO_3$ records^{17,18,21,22,24}. Although these precession signals seem to contrast across different records, $CaCO_3$ variability has been widely related to orbitally driven lysocline depth variations that resulted from precession controls on temperature and the carbon cycle^{17,18}. At diverse localities, LPEE enhanced $CaCO_3$ dissolution coincided with lighter $\delta^{13}C$ and $\delta^{18}O$ values on precession timescales^{17,65}. These variations were amplified during eccentricity maxima^{17,18,21,65}, which is also visible in the form of amplitude modulation patterns of precession in our $PC1_{dis}$ record (Fig. S16). This suggests that the $PC1_{dis}$ precession signal can be a useful indicator of the impacts of precession-related light carbon concentration/temperature variability on $CaCO_3$ dissolution. Accordingly, enhanced $CaCO_3$ dissolution, associated with higher temperatures and increased light carbon concentrations in the ocean/atmosphere, coincides with $PC1_{dis}$ precession maxima^{18,21,22,24,62} (Fig. 8c). The filtered HIRM-CFB precession signal is typically out of phase with that of the $PC1_{dis}$ record (Fig. 8c), which is confirmed by phase spectra (see Methods) that consistently indicate lag/lead relationships between ~ 3 kyr and ~ 10 kyr (Fig. 7). Out-of-phase HIRM-CFB precession with respect to $PC1_{dis}$ reveals that enhanced $CaCO_3$ dissolution, and its associated temperature and light carbon concentration increases, coincide with haematite formation/transportation reductions on precession timescales, which is a similar pattern to that identified for orbitally controlled Neogene-Quaternary sedimentation in Mediterranean zones^{47,63,64}.

Precession controls on $CaCO_3$ dissolution and temperature identified at Contessa Road^{21,24} suggest that precession-driven seasonality played a role in western Tethyan hydroclimate variability. Northern hemisphere summer insolation maxima and winter insolation minima during precession minima (perihelion in the northern hemisphere summer) are expected to induce summer temperature increases and winter temperature decreases in sub-tropical regions such as the proto-Mediterranean and Mediterranean zones⁶³. These precession-driven insolation maxima conditions have been indicated to promote enhanced $CaCO_3$ dissolution^{17,21} and intensify seasonal precipitation in Mediterranean zones^{47,64}. Hence, our finding of reduced haematite production during such times can be related to moisture increases and chemical weathering amplification, which promoted haematite precursor formation⁵⁶. During the opposite precession phase, reduced precession-driven seasonality coincides with $PC1_{dis}$ minima and HIRM-CFB maxima (Fig. 8c). This suggests that precession maxima conditions enhanced ferrihydrite transformation into haematite, which reveals strengthened aridity and likely expanded proto-Mediterranean semi-arid and arid zones in western Tethyan continental regions^{34,47,64}. This pattern explains the origins of the HIRM-CFB precession signal via aeolian dust deposition, which has been recognised as the dominant sedimentation mechanism that controlled haematite accumulation at Contessa Road^{44,48,49,57}.

Precession-related HIRM-CFB variability suggests that long and short eccentricity also impacted western Tethyan hydroclimates through amplitude modulation of precession. These eccentricity controls are indicated by the filtered HIRM-CFB short eccentricity signal, which consistently has high haematite contents that coincide with short eccentricity maxima in the ZB18a astronomical solution²³

and with short-lived LPEE carbon cycle perturbations (Fig. 8b). This pattern can be a partial result of high-amplitude precession cycles associated with short eccentricity maxima conditions, which strengthened insolation controls on ferrihydrite/haematite production with intensified wet phases that accelerated chemical weathering during precession-driven insolation maxima conditions, and subsequent periods with expanded arid zones that enhanced the ferrihydrite→haematite transformation. This orbitally forced mechanism, in conjunction with short-lived carbon cycle perturbations, systematically strengthened western Tethyan hydroclimate variability. Enhanced orbital controls on the hydrological cycle and/or non-linear hydroclimate responses to short-lived global warming events^{15,16} should have caused seasonal precipitation reductions that promoted predominantly dry conditions during HIRM-CFB short eccentricity maxima periods^{9,16,28,37}. Our finding of orbitally controlled dry/wet variations suggests considerable similarity between western Tethys LPEE hydroclimate variability and the well-documented Quaternary Mediterranean-type climate. Thus, we propose that LPEE hydroclimates of proto-Mediterranean regions were driven by winter storm track activity^{14,47} and/or by enhanced monsoon fluctuations^{16,33,66} that penetrated western Tethyan areas.

The filtered HIRM-CFB short eccentricity signal also contains intervals that are distinctly out of phase with the ZB18a astronomical solution (rectangles with dashed black lines in Fig. 8b). This visual observation is confirmed by lag/lead relationships of up to -77 kyr in $PC1_{dis}/HIRM-CFB$ phase spectra (Fig. 7) and indicates a contrasting HIRM-CFB pattern with respect to short-lived carbon cycle perturbations. Out-of-phase HIRM-CFB short eccentricity cycles occur mainly in coincidence with long eccentricity minima in the ZB18a astronomical solution²³. This may suggest that only a combination of high light carbon concentrations and enhanced precession-driven haematite production, which is expected to be driven partially by long eccentricity maxima, can generate hydroclimate variations recorded in the short eccentricity band¹⁵. However, short eccentricity maxima also coincide well with the ZB18a astronomical solution²³ in some Contessa Road intervals without short-lived carbon cycle perturbations (Fig. 8b). This might suggest that the HIRM-CFB record was not sufficiently sensitive to short eccentricity variations during intervals in which long eccentricity forcing reduced precession cycle amplitudes. Nevertheless, this interpretation would conflict with the out-of-phase short eccentricity cycles following the I1 and I2 events (Fig. 8b). Another hypothesis to explain the variable phase behaviour of the filtered HIRM-CFB short eccentricity signal is that Contessa Road haematite originated at different latitudes with contrasting orbitally forced hydroclimate conditions. However, this interpretation is not consistent with sedimentary provenance studies that indicate proto-Mediterranean continental zones as detrital material sources for Scaglia Rossa carbonates^{42,44}. Post-depositional authigenic pigmentary haematite formation could have disturbed orbital signals, but this does not seem to apply to Contessa Road, where magnetic minerals seem to have a mainly detrital origin. Finally, emergence of short eccentricity signals in other early Eocene hydroclimate records has been related partially to power transfer from precession to short eccentricity due to asymmetric climate system responses to insolation forcing (e.g., clipping¹⁵). We have no evidence to assess conclusively the significance of the HIRM-CFB short eccentricity cycles that are out of phase with the ZB18a astronomical solution²³. Hence, we leave this as an open question and instead focus on the amplified effects of short-lived carbon cycle perturbations and enhanced orbitally-driven seasonal contrast^{15,16} on western Tethyan aridification.

Carbon cycle controls on proto-Mediterranean hydroclimates

The impact of short-lived carbon cycle perturbations on LPEE hydroclimates indicates that the hydrological cycle changed over longer periods than those associated with orbital frequencies^{9,15,16,28}. The

Contessa Road magnetic mineral record has an unusual long-term pattern in which a gradual haematite content drop (HIRM-CFB reductions) coincided with its compositional enrichment in magnetic mineral fractions (higher B_{cr} values) (Fig. 5). This pattern can be explained by a gradual transition to drier western Tethys conditions, which inhibited chemical weathering and ferrihydrite production, but enhanced transformation of available ferrihydrite into haematite. This interpretation is consistent with modelling results that indicate that atmospheric circulation changes under high temperatures produced LPEE dry-drier sub-tropical conditions⁹. However, this interpretation also implies that contrasting wetter conditions would have been characterised by increased magnetic mineral contents and compositional prevalence of magnetite/maghemite over haematite. These relationships between magnetic mineral composition and content variability with respect to hydroclimate conditions are confirmed by PCA of M_{rs} -CFB, ARM-CFB, HIRM-CFB, S-ratio, and B_{cr} (referred to here as PCA_{arid} ; Fig. 9a, SI3c), which has a $PC1_{arid}$ (69% of data variance) with positive ARM-CFB, HIRM-CFB, M_{rs} -CFB, and S-ratio loadings, and a negative B_{cr} loading.

From $PC1_{arid}$ the wettest LPEE western Tethys conditions occurred during the EETZ (Fig. 9a). This interval with high detrital inputs (Fig. 5) indicates possible fluvial transport of terrigenous sediment to Contessa Road, which contrasts with the rest of the section in which aeolian dust deposition controlled detrital sedimentation^{44,48,49,57}. $PC1_{arid}$ has a gradual drop that mirrors $\delta^{13}C$, which suggests that the protracted transition to drier proto-Mediterranean zones was a response to the LPEE long-term carbon cycle perturbation and its associated higher temperatures^{12,20} (Fig. 9). Dry hydroclimates in these areas were especially pronounced during the PETM (Fig. 9a) and L1-L2 events. The ETM 2 and ETM 3 were also characterised by dry settings; however, these events have similar $PC1_{arid}$ values to other intervals that do not coincide with short-lived carbon cycle perturbations. These variable dry hydroclimate responses indicate that long-term warming exerted larger controls on western Tethyan hydroclimate variability compared to the short-lived global warming events, and suggests that seasonal precipitation systems (e.g., monsoons, storm tracks) may have had non-linear responses to LPEE light carbon injections^{15,16}.

Possible non-linear hydroclimate responses of proto-Mediterranean regions to LPEE light carbon injections are tested via estimation of hydroclimate recovery timescales. Irreversible $\delta^{13}C$ shifts from CIE conditions to more positive values across hyperthermal recovery phases coincide with $PC1_{arid}$ transitions from negative to more positive values (Fig. 9). These $PC1_{arid}$ changes allow us to constrain hydroclimate recovery timescales with -27 kyr and -24 kyr durations for the PETM and ETM 2, respectively. Hydroclimate recovery following these events is well defined by the beginning of wetter conditions for the PETM and by a less dry setting for the ETM 2. The ETM 3 may have had a similar -25 kyr-long hydroclimate recovery period that coincided with $\delta^{13}C$ recovery; nevertheless, the interrupted $PC1_{arid}$ record during the EELMZ (see Supplementary results) does not allow verification of the reliability of this estimate. The narrow range of hydroclimate recovery estimates for events with contrasting magnitudes^{13,22,25,26} allow us to suggest that optimised carbon removal following hyperthermal peak conditions^{19,27} also re-established the hydrological cycle to pre-event-like conditions, which confirms the non-linear response of western Tethyan hydroclimate drivers to carbon cycle perturbations. The -24-27-kyr-long hydroclimate recovery estimates also reveal that hydrological cycle changes associated with massive carbon cycle perturbations may last even longer than other detrimental impacts of global warming¹⁹ (e.g., ocean acidification), and indicate that increased temperatures, such as those induced by anthropogenic global warming, can disrupt hydroclimate variability for thousands of years.

Overall, we infer from the Contessa Road record that LPEE long-term and short-lived carbon cycle perturbations induced, in general,

dry-drier proto-Mediterranean hydroclimate conditions that disturbed orbitally driven dry-wet variations. Our estimates of hydroclimate recovery following peak hyperthermal conditions support model projections, which indicate that global warming can adversely impact the climate system for thousands of years. Along with model results^{9,28,35}, our documented dry-drier response of proto-Mediterranean zones to increased temperatures indicates future dry conditions in Mediterranean zones and suggests that an anthropogenic SSP 8.5 hothouse world can potentially cause extensive dry-land aridification in sub-tropical latitudes^{29,67}.

Methods

The Contessa Road section

The Cretaceous-Palaeogene Contessa Road section (lat. 43°22'47"N; long. 12°33'50"E) is a marine sedimentary section located northwest of the township of Gubbio, Italy. This section was deposited in the western Tethyan Umbria-Marche basin and records LPEE pelagic carbonate sedimentation of the Scaglia Rossa Formation⁴¹. Deposition of these LPEE carbonates occurred between magnetochrons C24r and C23r, and between calcareous nannofossil zones NP8/9 and NP12 over the ~30–48 m stratigraphic depth interval at Contessa Road (Fig. S1). The 0 m depth at Contessa Road coincides with the K/Pg boundary; positive depths correspond to younger strata²¹. CaCO₃-based and $\delta^{13}\text{C}$ -based astrochronological age models have been used to refine Contessa Road age constraints^{19,21,24}. These age models reveal that major hyperthermals such as the PETM, ETM 2 and ETM 3 are recorded

within marly layers at ~31.3 m, ~40 m, and ~46 m depths, respectively^{19,21} (Fig. S1). Piedrahita et al.¹⁹ developed the most recent LPEE chronology for Contessa Road. They initially divided the section into two outcrops (Fig. S1). Outcrop A ranges between 30 m and 33 m depth at Contessa Road and contains a PETM record, while outcrop B ranges from ~33 m to ~48 m depth at Contessa Road and contains records of the F, ETM 2, H2, I1, I2, ETM 3, L1 and L2 events^{19,21}. The J event is also indicated tentatively in this outcrop; however, its $\delta^{13}\text{C}$ expression is not well developed¹⁹ (Fig. S1; 19). Piedrahita et al.¹⁹ identified orbital signatures in high-resolution BR- χ and $\delta^{13}\text{C}$ records. BR- χ was interpreted to indicate CaCO₃ content changes, while $\delta^{13}\text{C}$ was associated with light carbon concentration variability. Therefore, BR- χ presents the same variations of detrital element patterns, and $\delta^{13}\text{C}$ anti-correlate with detrital element indices^{19,21,24,62}. Long and short eccentricity cycles within BR- χ and $\delta^{13}\text{C}$ were tuned to the ZB18a astronomical solution²³ (Fig. S2); hence, a CaCO₃ dissolution indicator such as PC1_{dis} represents the same variability described by Piedrahita et al.¹⁹. Tuning to the ZB18a astronomical solution allowed transfer of Contessa Road records from the depth domain to the time domain (Fig. S1, S2). Analyses for this study were performed on the same samples as Piedrahita et al.¹⁹; therefore, all of our records are presented in the time domain.

Sampling

The LPEE Contessa Road interval was sampled at 1-cm resolution in hyperthermals and in continuous 2-cm stratigraphic intervals in other parts of the section. Ca, CaCO₃ and $\delta^{13}\text{C}$ data for the LPEE Contessa

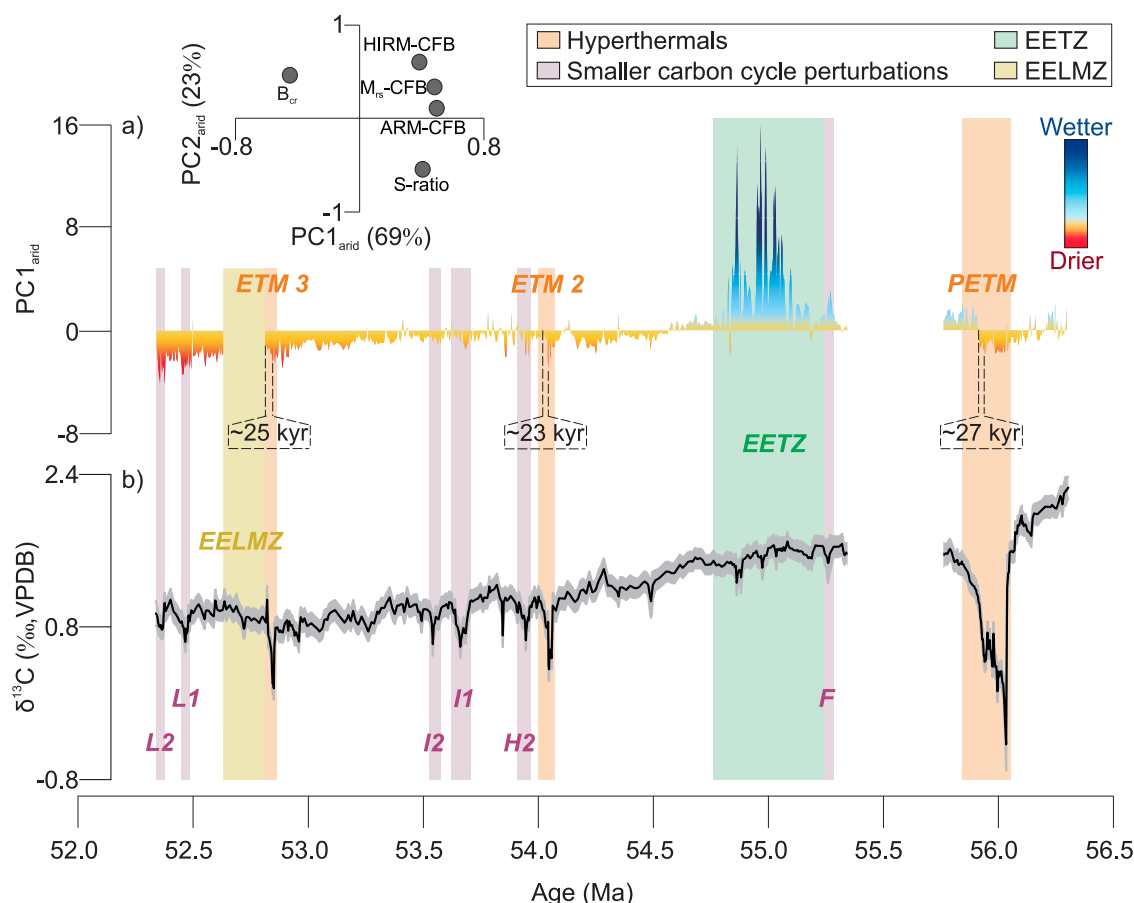


Fig. 9 | Hydroclimate variability of western Tethyan continental areas. a PC1_{arid}–PC2_{arid} plot and PC1_{arid} scores. The early Eocene low magnetisation zone (EELMZ) was excluded because of its anomalous magnetic mineral assemblage (see Supplementary information). **b** Contessa Road stable carbon isotope ($\delta^{13}\text{C}$) record presented in terms of mean (black) \pm 2 standard errors (SE) (grey shaded bands)¹⁹.

Hyperthermals (Palaeocene-Eocene Thermal Maximum (PETM), Eocene Thermal Maximum (ETM) 2 and ETM 3), smaller carbon cycle perturbations, the early Eocene terrigenous zone (EETZ), and the early Eocene low magnetisation zone (EELMZ) are indicated with orange, purple, green and yellow bands, respectively.

Road record were presented by Piedrahita et al.¹⁹. XRF Fe, Si and Ca results are from Piedrahita et al.²⁴ only for the PETM interval (outcrop A in Fig. S1); all remaining XRF, rock magnetic and SEM data were generated in this study at the Australian National University and the Chinese Academy of Sciences.

X-ray fluorescence measurements

Samples were cut to expose flat surfaces for XRF measurements. Analyses were made using a third generation Avaatech XRF Core Scanner with a Canberra X-PIPS silicon drift detector operated at 10 kV (current = 0.5 mA, count time = 60 s, no filter) and 30 kV (current = 0.5 mA, count time = 60 s, Pd-Thick filter). All samples were cleaned and fixed over plastic holders for discrete XRF measurements using a 16 mm² sample area. Sample spacing in the core scan table was ~20 cm to avoid interference between measurements. Standards were run between measurement sets to test measurement reliability. Raw X-ray spectra were analysed via iterative least squares analysis in the Win Axil software from Canberra Eurisys.

Rock magnetism

Samples were cut into ~1 cm cubes for ARM and hysteresis measurements. ARM measurements were made with a 2 G Enterprises cryogenic magnetometer. ARMs were induced using a 140-mT alternating field and a 0.05-mT direct current bias field. Hysteresis loops were measured with a Princeton Measurements Corporation vibrating sample magnetometer 3900 to ±1 T maximum fields with a 2-mT field step. Saturation remanent magnetisation (M_{rs}), saturation magnetisation (M_s), coercivity (B_c), low-field χ (χ_{lf}), and high-field χ (χ_{hf}) were calculated from hysteresis loops. Using the upper ($M^+(H)$) and lower ($M^-(H)$) hysteresis branches, we estimated a symmetric remanent hysteretic magnetisation derived curve (M_{rh}) from $(1)M_{rh}(H) = (M^+(H) - M^-(H))/2$, where H corresponds to the magnetic field strength and M to magnetisation⁶⁸. Using the M_{rh} curve, we estimated $B_{rh} \approx B_c$ as $(2)M_{rh}(B_{rh}) = (M_{rh}(0T))/2$, HIRM $(3)(M_{rh}(1.0T) - M_{rh}(0.3T))$, L-ratio $(4)(M_{rh}(0.3T)/M_{rh}(0.1T))$, and S-ratio $(5)(M_{rh}(0.3T)/M_{rh}(0T))$. We used Burr type XII distributions⁶⁸ of M_{rh} curves to unmix magnetic mineral components to separate coercivity components (see Supplementary results).

Temperature-dependent magnetic analyses were made for representative samples. Samples were crushed for χ -T measurements, which were performed in an argon atmosphere with an AGICO MF1-KFA Kappabridge equipped with a CS-3 furnace. Three-axis thermal demagnetisation was performed using samples that were cut into rectangular cuboids. Soft-, medium- and high-coercivity isothermal remanent magnetisation fractions were induced with direct current fields of 0.05 T, 0.3 T and 2.7 T along three orthogonal sample axes. Samples were then demagnetised thermally in an ASC TD-48SC oven and measured on a 2 G Enterprises cryogenic magnetometer.

Bulk-rock (BR) magnetic mineral concentration parameters were normalised with respect to sample mass. An example of these calculations is given by $BR \cdot M_{rs}$ in the following equation:

$$Br - M_{rs}(Am^2 kg^{-1}) = \frac{M_{rs}(Am^2)}{Sample\ mass(kg)} \quad (6)$$

Carbonate-free basis (CFB) magnetic mineral concentration parameters were estimated using the high-resolution $CaCO_3$ record of Piedrahita et al.¹⁹, which makes it possible to subtract mathematically the $CaCO_3$ content of each analysed sample for subsequent data normalisation. An example of CFB calculations is given by M_{rs} -CFB as follows:

$$M_{rs} - CFB(Am^2 kg^{-1}) = \frac{M_{rs}(Am^2)}{(Sample\ mass(kg) * (100\% - CaCO_3(\%)))} \quad (7)$$

where (8) $(100\% - CaCO_3(\%))$ is the sample mass percentage that does not consist of $CaCO_3$.

Principal component analysis (PCA)

Different datasets were standardised to perform principal component analysis (PCA). An initial PCA was performed using detrital and biogenic XRF elements (referred to here as PCA_{dis}) to identify $CaCO_3$ dissolution patterns at Contessa Road. A second PCA was carried out with XRF elements, CFB magnetic mineral concentration parameters, B_{cr} and S-ratio (referred to here as PCA_{all}) to assess relationships between terrigenous inputs, $CaCO_3$ dissolution and magnetic mineral composition on Contessa Road carbonates. Finally, a third PCA was performed using M_{rs} -CFB, ARM-CFB, HIRM-CFB, B_{cr} and S-ratio (referred to here as PCA_{arid}) to characterise magnetic mineral content and compositional variations associated with western Tethyan hydroclimate variability.

Spectral analysis

PCI_{dis} and HIRM-CFB were divided into intervals to avoid the EETZ and the EELMZ. These two periods had different sedimentation patterns to those that record orbitally controlled $CaCO_3$ dissolution cycles through the rest of the Contessa Road section²¹. Three intervals (PETM, post EETZ-pre EELMZ interval and post EELMZ interval) are treated separately to explore orbital signals at Contessa Road. All records were interpolated to the average sampling resolution of each interval, which varies between ~2 kyr and ~4 kyr. All records were then detrended with locally estimated scatterplot smoothing (LOESS) filters and local regression windows equivalent to 35% of record lengths. Spectral analyses were carried out using the Acycle Software⁶⁹ with the periodogram and multi-taper methods. Short eccentricity and precession signals were isolated using Gaussian bandpass filters with bandwidths of 0.010 ± 0.003 (1 σ) cycles kyr⁻¹ (~75–140 kyr) for short eccentricity, and 0.044 ± 0.010 (1 σ) cycles kyr⁻¹ (~18–29 kyr) for precession. All filtered signals were then normalised between -1 and 1 to allow amplitude comparisons between orbital signals of different intervals.

Cross-spectral analysis was performed using the Lomb-Scargle Fourier transform in the RedFit-X software⁷⁰. This software was used to generate squared coherency and phase spectra for PCI_{dis} and HIRM-CFB for each interval in which orbital signals are studied—i.e., the PETM, post EETZ-Pre EELMZ and post EELMZ intervals.

Scanning electron microscope observations

Representative samples were cut, embedded in an epoxy resin mount, and polished to make cross sections. Samples were then carbon coated to produce a conductive layer for SEM observations with a Thermo Fisher Apreo SEM equipped with a Bruker QUANTAX energy dispersive X-ray spectrometer. These instruments allow the identification of morphological features and chemical composition of samples. SEM observations were performed with a ~10 mm working distance, 15 kV accelerating voltage and 6.4 nA current.

Data availability

All data generated in this study are provided in the Supplementary Information/Source Data file. Source data are provided for all rock magnetic and X-ray fluorescence measurements. Source data are provided with this paper.

Code availability

The PCA code used in this manuscript is available at FigShare (<https://doi.org/10.6084/m9.figshare.25522990>).

References

1. Archer, D. et al. Atmospheric lifetime of fossil fuel carbon dioxide. *Annu. Rev. Earth Planet. Sci.* **37**, 117–134 (2009).

2. IPCC. Climate Change 2021: The Physical Science Basis. Contribution of Working Group I to the Sixth Assessment Report of the Intergovernmental Panel on Climate Change, in Masson-Delmotte, V. et al. (Eds.), Cambridge University Press, Cambridge, United Kingdom and New York, NY, USA (2021).
3. Milly, P. C. D., Dunne, K. A. & Vecchia, A. V. Global pattern of trends in streamflow and water availability in a changing climate. *Nature* **438**, 347–350 (2005).
4. Ault, T. R., Cole, J. E., Overpeck, J. T., Pederson, G. T. & Meko, D. M. Assessing the risk of persistent drought using climate model simulations and paleoclimate data. *J. Clim.* **27**, 7529–7549 (2014).
5. Moon, H., Gudmundsson, L. & Seneviratne, S. I. Drought persistence errors in global climate models. *J. Geophys. Res. Atmos.* **123**, 3483–3496 (2018).
6. Hobeichi, S. et al. Reconciling historical changes in the hydrological cycle over land. *NPJ Clim. Atmos. Sci.* **5**, 17 (2022).
7. Schuster, M. et al. Chad basin: paleoenvironments of the Sahara since the late Miocene. *C. R. -Geosc.* **341**, 603–611 (2009).
8. Feng, R. et al. Past terrestrial hydroclimate sensitivity controlled by Earth system feedbacks. *Nat. Commun.* **13**, 1306 (2022).
9. Cramwinckel, M. J. et al. Global and zonal-mean hydrological response to early Eocene warmth. *Paleoceanogr. Paleoclimatol.* **38**, e2022PA004542 (2023).
10. Zeebe, R. E. Time-dependent climate sensitivity and the legacy of anthropogenic greenhouse gas emissions. *Proc. Natl Acad. Sci. USA* **110**, 13739–13744 (2013).
11. Burke, K. D. et al. Pliocene and Eocene provide best analogs for near-future climates. *Proc. Natl Acad. Sci. USA* **115**, 13288–13293 (2018).
12. Westerhold, T. et al. An astronomically dated record of Earth's climate and its predictability over the last 66 million years. *Science* **369**, 1383–1387 (2020).
13. Zeebe, R. E., Zachos, J. C. & Dickens, G. R. Carbon dioxide forcing alone insufficient to explain Palaeocene–Eocene Thermal Maximum warming. *Nat. Geosci.* **2**, 576–580 (2009).
14. Tierney, J. E. et al. Spatial patterns of climate change across the Paleocene-Eocene Thermal Maximum. *Proc. Natl Acad. Sci. USA* **119**, e2205326119 (2022).
15. Walters, A. P. et al. Climate system asymmetries drive eccentricity pacing of hydroclimate during the early Eocene greenhouse. *Sci. Adv.* **9**, eadg8022 (2023).
16. Meijer, N. et al. Proto-monsoon rainfall and greening in Central Asia due to extreme early Eocene warmth. *Nat. Geosci.* **17**, 158–164 (2024).
17. Littler, K., Röhl, U., Westerhold, T. & Zachos, J. C. A high-resolution benthic stable-isotope record for the South Atlantic: implications for orbital-scale changes in Late Paleocene-Early Eocene climate and carbon cycling. *Earth Planet. Sci. Lett.* **401**, 18–30 (2014).
18. Zeebe, R. E., Westerhold, T., Littler, K. & Zachos, J. C. Orbital forcing of the Paleocene and Eocene carbon cycle. *Paleoceanography* **32**, 440–465 (2017).
19. Piedrahita, V. A. et al. Accelerated light carbon sequestration following late Paleocene-early Eocene carbon cycle perturbations. *Earth Planet. Sci. Lett.* **604**, 117992 (2023).
20. Komar, N., Zeebe, R. E. & Dickens, G. R. Understanding long-term carbon cycle trends: the late Paleocene through the early Eocene. *Paleoceanography* **28**, 650–662 (2013).
21. Galeotti, S. et al. Orbital chronology of Early Eocene hyperthermals from the Contessa Road section, central Italy. *Earth Planet. Sci. Lett.* **290**, 192–200 (2010).
22. Zachos, J. C., McCarren, H., Murphy, B., Röhl, U. & Westerhold, T. Tempo and scale of late Paleocene and early Eocene carbon isotope cycles: implications for the origin of hyperthermals. *Earth Planet. Sci. Lett.* **299**, 242–249 (2010).
23. Zeebe, R. E. & Lourens, L. J. Solar system chaos and the Paleocene-Eocene boundary age constrained by geology and astronomy. *Science* **365**, 926–929 (2019).
24. Piedrahita, V. A. et al. Orbital phasing of the Paleocene-Eocene Thermal Maximum. *Earth Planet. Sci. Lett.* **598**, 117839 (2022).
25. Gutjahr, M. et al. Very large release of mostly volcanic carbon during the Palaeocene-Eocene Thermal Maximum. *Nature* **548**, 573–577 (2017).
26. Harper, D. T. et al. The magnitude of surface ocean acidification and carbon release during Eocene Thermal Maximum 2 (ETM-2) and the Paleocene-Eocene Thermal Maximum (PETM). *Paleoceanogr. Paleoclimatol.* **35**, e2019PA003699 (2020).
27. Komar, N. & Zeebe, R. E. Redox-controlled carbon and phosphorus burial: a mechanism for enhanced organic carbon sequestration during the PETM. *Earth Planet. Sci. Lett.* **479**, 71–82 (2017).
28. Carmichael, M. J. et al. Hydrological and associated biogeochemical consequences of rapid global warming during the Paleocene-Eocene Thermal Maximum. *Glob. Planet. Change* **157**, 114–138 (2017).
29. Held, I. M. & Soden, B. J. Robust responses of the hydrological cycle to global warming. *J. Clim.* **19**, 5686–5699 (2006).
30. Bolle, M. P. & Adatte, T. Palaeocene-early Eocene climatic evolution in the Tethyan realm: clay mineral evidence. *Clay Min.* **36**, 249–261 (2001).
31. Schmitz, B. & Pujalte, V. Abrupt increase in seasonal extreme precipitation at the Paleocene-Eocene boundary. *Geology* **35**, 215–218 (2007).
32. Dallanave, E., Agnini, C., Muttoni, G. & Rio, D. Paleocene magneto-biostratigraphy and climate-controlled rock magnetism from the Belluno Basin, Tethys Ocean, Italy. *Palaeogeogr. Palaeoclimatol. Palaeoecol.* **337**, 130–142 (2012).
33. Huber, M. & Goldner, A. Eocene monsoons. *J. Asian Earth Sci.* **44**, 3–23 (2012).
34. Korasidis, V. A., Wing, S., Shields, J. & Kiehl, J. T. Global changes in terrestrial vegetation and continental climate during the Paleocene-Eocene Thermal Maximum. *Paleoceanogr. Paleoclimatol.* **37**, e2021PA004325 (2022).
35. Williams, C. J. et al. African hydroclimate during the early Eocene from the DeepMIP simulations. *Paleoceanogr. Paleoclimatol.* **37**, e2022PA004419 (2022).
36. Pagani, M. et al. Arctic hydrology during global warming at the Palaeocene/Eocene thermal maximum. *Nature* **442**, 671–675 (2006).
37. Harper, D. T. et al. Subtropical sea-surface warming and increased salinity during Eocene Thermal Maximum 2. *Geology* **46**, 187–190 (2018).
38. Willard, D. A. et al. Arctic vegetation, temperature, and hydrology during Early Eocene transient global warming events. *Glob. Planet. Change* **178**, 139–152 (2019).
39. Pogge von Strandmann, P. A. et al. Lithium isotope evidence for enhanced weathering and erosion during the Paleocene-Eocene Thermal Maximum. *Sci. Adv.* **7**, eab4224 (2021).
40. Abels, H. A. et al. Environmental impact and magnitude of paleosol carbonate carbon isotope excursions marking five early Eocene hyperthermals in the Bighorn Basin, Wyoming. *Clim.* **12**, 1151–1163 (2016).
41. Giusberti, L., Coccioni, R., Sprovieri, M. & Tateo, F. Perturbation at the sea floor during the Paleocene-Eocene Thermal Maximum: evidence from benthic foraminifera at Contessa Road, Italy. *Mar. Micropaleontol.* **70**, 102–119 (2009).
42. Aguirre-Palafox, L. E., Alvarez, W., Boschi, S., Martin, E. & Schmitz, B. Zircon provenance analysis from Lower Paleocene pelagic limestones of the Bottaccione section at Gubbio (Umbria-Marche basin,

- Italy), in: Koeberl, C. & Bice, D. M. (Eds.), 250 Million Years of Earth History in Central Italy: Celebrating 25 Years of the Geological Observatory of Coldigioco. *Geol. Soc. Am. Spec. Pap.* **542**, 159–174 (2019).
43. Coccioni, R. et al. An integrated stratigraphic record of the Palaeocene-lower Eocene at Gubbio (Italy): new insights into the early Palaeogene hyperthermals and carbon isotope excursions. *Terra Nova* **24**, 380–386 (2012).
 44. Coccioni, R. et al. Paleoenvironmental signature of the Selandian–Thanetian transition event (STTE) and Early Late Paleocene Event (ELPE) in the Contessa Road section (western Neo-Tethys). *Palaeogeogr. Palaeoclimatol. Palaeoecol.* **523**, 62–77 (2019).
 45. Endo, H. & Kitoh, A. Thermodynamic and dynamic effects on regional monsoon rainfall changes in a warmer climate. *Geophys. Res. Lett.* **41**, 1704–1711 (2014).
 46. Seager, R. et al. Causes of increasing aridification of the Mediterranean region in response to rising greenhouse gases. *J. Clim.* **27**, 4655–4676 (2014).
 47. Bosmans, J. H. C. et al. Precession and obliquity forcing of the freshwater budget over the Mediterranean. *Quat. Sci. Rev.* **123**, 16–30 (2015).
 48. Abrajevitch, A., Font, E., Florindo, F. & Roberts, A. P. Asteroid impact vs. Deccan eruptions: the origin of low magnetic susceptibility beds below the Cretaceous–Paleogene boundary revisited. *Earth Planet. Sci. Lett.* **430**, 209–223 (2015).
 49. Sinnesael, M. et al. High-resolution multiproxy cyclostratigraphic analysis of environmental and climatic events across the Cretaceous–Paleogene boundary in the classic pelagic succession of Gubbio (Italy), in: Menichetti, M., Coccioni, R. & Montanari, A. (Eds.), The Stratigraphic Record of Gubbio: Integrated Stratigraphy of the Late Cretaceous–Paleogene Umbria–Marche Pelagic Basin. *Geol. Soc. Am. Spec. Pap.* **524**, 115–137 (2016).
 50. Larrasoana, J. C. et al. Magnetotactic bacterial response to Antarctic dust supply during the Palaeocene–Eocene thermal maximum. *Earth Planet. Sci. Lett.* **333**, 122–133 (2012).
 51. Roberts, A. P. et al. Magnetic properties of pelagic marine carbonates. *Earth-Sci. Rev.* **127**, 111–139 (2013).
 52. Liu, Q. et al. Temperature dependence of magnetic susceptibility in an argon environment: implications for pedogenesis of Chinese loess/palaeosols. *Geophys. J. Int.* **161**, 102–112 (2005).
 53. Özdemir, Ö. & Banerjee, S. K. High temperature stability of maghemite ($\gamma\text{-Fe}_2\text{O}_3$). *Geophys. Res. Lett.* **11**, 161–164 (1984).
 54. Lowrie, W. Identification of ferromagnetic minerals in a rock by coercivity and unblocking temperature properties. *Geophys. Res. Lett.* **17**, 159–162 (1990).
 55. Jiang, Z. et al. The magnetic and color reflectance properties of hematite: from Earth to Mars. *Rev. Geophys.* **60**, e2020RG000698 (2022).
 56. Zhang, Q. et al. Mechanism for enhanced eolian dust flux recorded in North Pacific Ocean sediments since 4.0 Ma: aridity or humidity at dust source areas in the Asian interior? *Geology* **48**, 77–81 (2020).
 57. Channell, J. E. T., Freeman, R., Heller, F. & Lowrie, W. Timing of diagenetic haematite growth in red pelagic limestones from Gubbio (Italy). *Earth Planet. Sci. Lett.* **58**, 189–201 (1982).
 58. Roberts, A. P. Magnetic mineral diagenesis. *Earth-Sci. Rev.* **151**, 1–47 (2015).
 59. Kodama, K. P. *Paleomagnetism of Sedimentary Rocks: Process and Interpretation*. Wiley-Blackwell, Oxford, 157 (2012).
 60. Liu, Y., Kissel, C., Mazaud, A., Pan, Y. & Li, J. Glacial-interglacial circulation and climatic changes in the South Indian Ocean (Kerguelen Plateau region) recorded by detrital and biogenic magnetic minerals. *J. Geophys. Res. Solid Earth* **128**, e2023JB027741 (2023).
 61. Li, J. et al. Classification of a complexly mixed magnetic mineral assemblage in Pacific Ocean surface sediment by electron microscopy and supervised magnetic unmixing. *Front. Earth Sci.* **8**, 609058 (2020).
 62. Francescone, F. et al. A 9 million-year-long astrochronological record of the early-middle Eocene corroborated by seafloor spreading rates. *Geol. Soc. Am. Bull.* **131**, 499–520 (2018).
 63. Rohling, E. J., Marino, G. & Grant, K. M. Mediterranean climate and oceanography, and the periodic development of anoxic events (sapropels). *Earth-Sci. Rev.* **143**, 62–97 (2015).
 64. Kutzbach, J. E. et al. African climate response to orbital and glacial forcing in 140,000-y simulation with implications for early modern human environments. *Proc. Natl Acad. Sci.* **117**, 2255–2264 (2020).
 65. Barnet, J. S. K. et al. A high-fidelity benthic stable isotope record of late Cretaceous–early Eocene climate change and carbon-cycling. *Paleoceanogr. Paleoclimatology*. **34**, 672–691 (2019).
 66. Licht, A. et al. Asian monsoons in a late Eocene greenhouse world. *Nature* **513**, 501–506 (2014).
 67. Sherwood, S. & Fu, Q. A drier future? *Science* **343**, 737–739 (2014).
 68. Zhao, X., Fujii, M., Suganuma, Y., Zhao, X. & Jiang, Z. Applying the Burr type XII distribution to decompose remanent magnetization curves. *J. Geophys. Res. Solid Earth* **123**, 8298–8311 (2018).
 69. Li, M., Hinnov, L. & Kump, L. Acycle: time-series analysis software for paleoclimate research and education. *Comput. Geosci.* **127**, 12–22 (2019).
 70. Ólafsdóttir, K. B., Schulz, M. & Mudelsee, M. REDFIT-X: cross-spectral analysis of unevenly spaced paleoclimate time series. *Comput. Geosci.* **91**, 11–18 (2016).

Acknowledgements

This study was supported financially by the National Natural Science Foundation of China (grants no. 42225402, 41920104009 and 42388101 to J.L.), the International postdoctoral exchange fellowship program–Talent introduction program of the Chinese Academy of Science (grant to V.A.P.), and by the Australian Research Council (grant DP200100765 to A.P.R. and D.H., and grant DE190100042 to K.M.G.).

Author contributions

V.A.P. led the research and writing. V.A.P., A.P.R., E.J.R., D.H., and S.G., designed the study. F.F., K.M.G. and J.L. added context to interpretation and writing. V.A.P., X.Z., K.M.G., P.H. J.L. helped with experiment development and data refinement. V.A.P., A.P.R., E.J.R., D.H., X.Z., S.G., F.F., K.M.G. P.H. and J.L. assisted in producing this manuscript.

Competing interests

The authors declare no competing interests.

Additional information

Supplementary information The online version contains supplementary material available at <https://doi.org/10.1038/s41467-024-51430-6>.

Correspondence and requests for materials should be addressed to Jinhua Li.

Peer review information *Nature Communications* thanks Ran Feng and the other, anonymous, reviewers for their contribution to the peer review of this work. A peer review file is available.

Reprints and permissions information is available at <http://www.nature.com/reprints>

Publisher's note Springer Nature remains neutral with regard to jurisdictional claims in published maps and institutional affiliations.

Open Access This article is licensed under a Creative Commons Attribution-NonCommercial-NoDerivatives 4.0 International License, which permits any non-commercial use, sharing, distribution and reproduction in any medium or format, as long as you give appropriate credit to the original author(s) and the source, provide a link to the Creative Commons licence, and indicate if you modified the licensed material. You do not have permission under this licence to share adapted material derived from this article or parts of it. The images or other third party material in this article are included in the article's Creative Commons licence, unless indicated otherwise in a credit line to the material. If material is not included in the article's Creative Commons licence and your intended use is not permitted by statutory regulation or exceeds the permitted use, you will need to obtain permission directly from the copyright holder. To view a copy of this licence, visit <http://creativecommons.org/licenses/by-nc-nd/4.0/>.

© The Author(s) 2024